Pattern Selection in Faraday Waves

Peilong Chen[1] and Jorge Viñals[1,2]
[1]*Supercomputer Computations Research Institute, Florida State University, Tallahassee, Florida 32306-4130*
[2]*Department of Chemical Engineering, FAMU-FSU College of Engineering, Tallahassee, Florida 32310*
(Received 10 February 1997)

We present a systematic nonlinear theory of pattern selection for parametric surface waves (Faraday waves), not restricted to fluids of low viscosity. A standing wave amplitude equation is derived from the Navier-Stokes equation that is of gradient form. The associated Lyapunov function is calculated for different regular patterns to determine the selected pattern near threshold as a function of a damping parameter γ. For $\gamma \sim 1$, we show that a single wave (or stripe) pattern is selected. For $\gamma \ll 1$, we predict patterns of square symmetry in the capillary regime, a sequence of sixfold (hexagonal), eightfold,... in the mixed gravity-capillary regime, and stripe patterns in the gravity dominated regime. [S0031-9007(97)04216-6]

PACS numbers: 47.20.Ky, 47.35.+i, 47.54.+r

Parametrically driven surface waves (also known as Faraday waves) can be excited on the free surface of a fluid layer when periodically vibrated in the direction normal to the surface at rest. Above a critical value of the driving amplitude, the planar surface becomes unstable to a pattern of standing waves [1]. Patterns of various symmetries have been observed in large aspect ratio systems (large lateral size of the fluid layer compared to the wavelength of the waves) depending on the driving frequency and fluid properties (viscosity, surface tension and density). They include single standing waves (parallel stripe patterns), two waves at a 90° angle (square patterns), and more recently hexagonal, eightfold and tenfold patterns [2–5]. We present a weakly nonlinear analysis of the equations governing fluid motion that predicts standing wave patterns with these symmetries in regions of parameters that are in quantitative agreement with experiments [4,5].

We consider an incompressible and viscous fluid layer that extends to $z = -\infty$, is unbounded in the x-y direction, and that at rest has a free surface at $z = 0$. The equation governing fluid motion under periodic vibration is

$$\partial_t \mathbf{u} + (\mathbf{u} \cdot \nabla)\mathbf{u} = -\frac{1}{\rho}\nabla p + \nu\nabla^2\mathbf{u} + g_z(t)\hat{\mathbf{e}}_z , \quad (1)$$

with $\mathbf{u}$ the velocity field, p the pressure, ρ and ν the density and kinematic viscosity of the fluid, respectively, and $g_z(t) = -g - f\cos\omega t$ the effective gravity. For f below the threshold of instability, the base state is $\mathbf{u} = 0$ and $p = \rho g_z(t) z$. Although we use mostly dimensional variables in the analysis below, the natural dimensionless variables involve $\omega_0 = \omega/2$ as the inverse time scale, k_0 defined from the linear dispersion relation of surface waves $\omega_0^2 = gk_0 + \sigma k_0^3/\rho$ as the inverse length scale, and include a damping parameter $\gamma = 2\nu k_0^2/\omega_0$, the gravity wave $G = gk_0/\omega_0^2$ and capillary wave $\Sigma = \sigma k_0^3/\rho\omega_0^2$ contributions to the dispersion relation, and the dimensionless amplitude of the driving acceleration $\Delta = fk_0/4\omega_0^2$.

Progress in deriving suitable amplitude equations for Faraday waves has proved difficult, in part due to the existence of two small parameters that are not independent: the reduced distance away from threshold, ϵ, and γ. For finite γ and small ϵ, viscous dissipation is the dominant source of nonlinear wave saturation. In the inviscid limit, on the other hand, cubic terms are prohibited in the amplitude equation, and other mechanisms for saturation of the wave have to be invoked [1]. Early work on Faraday waves was based on a Hamiltonian description for the ideal (inviscid) fluid, and treated viscous effects as a regular perturbation in which damping was assumed to result solely from irrotational bulk flow [6,7]. At linear order in the surface variables, the dominant viscous contribution is of order γ, and results entirely from viscous damping of the irrotational flow. The rotational contribution is of higher order ($\gamma^{3/2}$) [8]. At the nonlinear level, however, the contribution from rotational flow to cubic terms in the amplitude equation given below is of the same order as that of irrotational flow (order γ).

Another important qualitative feature of Faraday waves concerns three wave (or triad) resonant interactions. Three wave interactions are generically permitted when the dispersion relation satisfies $\partial^2\omega/\partial k^2 \geq 0$, as is the case in the capillary regime. For gravity waves, $\partial^2\omega/\partial k^2 < 0$ and only four wave interactions are possible. Although sign invariance of the standing wave amplitude equation prohibits quadratic nonlinear terms, triad resonant interactions are possible through linearly stable modes [3,9]. The resonant angle is largest for $\Sigma = 1$ (capillary limit), and goes to zero at $\Sigma = 1/3$ [10]. If the stable modes are only weakly damped ($\gamma \ll 1$), triad resonant interactions become dominant and effectively determine the symmetry of the selected pattern. In particular, they lead to a sequence of high-symmetry patterns in the vicinity of $\Sigma = 1/3$ [10].

Both issues were partially addressed recently in [10]. The governing equations and boundary conditions were expanded in powers of γ and further simplified (in an uncontrolled way) by neglecting all terms proportional to γ which were nonlinear in the surface variables. The

 0031-9007/97/79(14)/2670(4)$10.00

approximate equations predict bifurcations to square and higher-symmetry patterns, but because of the underlying uncontrolled approximation, their region of validity is difficult to assess. In addition, they fail to yield the observed stripe patterns at moderate values of γ. We present here a general calculation that overcomes these difficulties, and that leads to the experimentally observed regular (periodic or quasiperiodic) standing wave patterns above onset.

We first eliminate the explicit dependence on the pressure in Eq. (1) by taking $-\nabla \times \nabla\times$ to obtain

$$\partial_t \nabla^2 \mathbf{u} - \nu \nabla^2 \nabla^2 \mathbf{u} = \nabla \times \nabla \times (\mathbf{u} \cdot \nabla)\mathbf{u} .$$

Here the continuity equation $\nabla \cdot \mathbf{u} = 0$ has also been used. The position of the free surface is denoted by $\zeta(x, y)$, the unit normal is $\hat{\mathbf{n}} = (-\partial_x \zeta, -\partial_y \zeta, 1)/\|(-\partial_x \zeta, -\partial_y \zeta, 1)\|$, and the two tangential unit vectors are $\hat{\mathbf{t}}_1 = (1, 0, \partial_x \zeta)/\|(1, 0, \partial_x \zeta)\|$ and $\hat{\mathbf{t}}_2 = (0, 1, \partial_y \zeta)/\|(0, 1, \partial_y \zeta)\|$. Besides the null conditions at $z = -\infty$, there are four boundary conditions to be satisfied at the free surface,

$$\begin{aligned} \partial_t \zeta + (\mathbf{u} \cdot \nabla_H)\zeta &= w|_{z=\zeta} , \\ \hat{\mathbf{t}}_m \cdot \mathbf{T} \cdot \hat{\mathbf{n}}|_{z=\zeta} &= 0, \qquad m = 1, 2 , \\ \hat{\mathbf{n}} \cdot \mathbf{T} \cdot \hat{\mathbf{n}}|_{z=\zeta} &= 2H\sigma , \end{aligned}$$

with $\nabla_H \equiv \hat{\mathbf{e}}_x \partial_x + \hat{\mathbf{e}}_y \partial_y$, $\mathbf{T}$ the stress tensor with components $T_{ij} = [-p - \rho g_z(t) z]\delta_{ij} + \rho\nu(\partial_j u_i + \partial_i u_j)$, σ the surface tension, and $2H$ the mean curvature of the free surface [11].

In order to study the linear stability of a subharmonic standing wave we introduce [12]

$$w_0 = \cos(kx) \sum_{j=1,3,5,\ldots} e^{ji\omega t/2} w_0^j(z) A_j + \text{c.c.} ,$$

where w_0 is the z component of the velocity field, and a similar expansion for ζ_0. Substitution into the linearized equation of motion, $(\partial_t \nabla^2 - \nu \nabla^2 \nabla^2) w_0 = 0$, and into the linearized kinematic and tangential stress boundary conditions, $\partial_t \zeta_0 - w_0 = 0$ and $(\nabla_H^2 - \partial_z^2) w_0 = 0$ yields

$$w_0^j(z) = (\tfrac{1}{2} ji\omega + 2\nu k^2) e^{kz} - 2\nu k^2 e^{q_j z},$$

with $q_j^2 \equiv k^2 + ji\omega/2\nu$. The first and second terms in the right-hand side arise from the irrotational and rotational flow components, respectively.

The critical amplitude f_0 is determined by the linearized normal stress boundary condition, which is, after using the momentum equation to eliminate p_0,

$$[2\nu\nabla_H^2 - (\partial_t - \nu\nabla^2)]\partial_z w_0 + \left(g - \frac{\sigma}{\rho}\nabla_H^2 + f\cos\omega t\right)\nabla_H^2 \zeta_0 = 0 .$$

Note that we do not use $\sin \omega t$ to avoid the complication due to its odd parity under time reversal. By substituting w_0 and ζ_0 into the above equation, we note that the term $2\nu\nabla_H^2 \partial_z w_0$, when acting on the irrotational flow component (e^{kz}), yields a contribution at low viscosity that scales as ν, whereas the rotational contribution (from $e^{q_j z}$) scales as $\nu^{3/2}$. The remaining term $(\partial_t - \nu\nabla^2)\partial_z w_0$ is simply equal to $-\omega^2$. Explicitly, we find the following hierarchy for each harmonic $e^{ji\omega t/2}$:

$$\begin{aligned} H_1 A_1 - f A_1^* - f A_3 &= 0 , \\ H_3 A_3 - f A_1 - f A_5 &= 0 , \\ H_5 A_5 - f A_3 - f A_7 &= 0, \ldots , \end{aligned} \tag{2}$$

with $H_j \equiv 2\nu^2[4q_j k^2 - \frac{1}{k}(q_j^2 + k^2)^2] - 2g - 2\sigma k^2/\rho$. By truncating Eq. (2) at some A_n, the system can be solved numerically as an eigenvalue problem. This is indeed what was done by Kumar and Tuckerman [12]. However, we observe that after truncation at A_n, $A_n = fA_{n-2}/H_n, A_{n-2} = fA_{n-4}/(H_{n-2} - \frac{f^2}{H_n}), \ldots$. Therefore the entire set of equations can be rewritten as

$$\left(H_1 - \frac{f^2}{H_3 - \frac{f^2}{H_5 - \ldots}}\right) A_1 - f A_1^* \equiv \bar{H}_1(k, f) A_1 - f A_1^* = 0 ,$$

so that for a given wave number k, the threshold of instability f_0 is given implicitly by $f_0 = |\bar{H}_1(k, f_0)|$. The complex amplitude A_j can be recursively obtained from Eq. (2) up to a real factor. For an infinite system the critical wave number k_{onset} is the wave number that corresponds to the lowest value of f_0. In the limit of low viscous damping, $\gamma \ll 1$, and k near k_{onset}, Δ_{onset} can be given explicitly as

$$\Delta_{\text{onset}} = \gamma - \frac{1}{2}\gamma^{3/2} + \frac{11 - 2G}{8(3 - 2G)}\gamma^{5/2} + \ldots ,$$

with $0 \le G \le 1$ by definition. While previous low damping calculations [6,10] only used the linear term to determine the location of the threshold, the first correction $-\frac{1}{2}\gamma^{3/2}$ can be a sizable contribution (e.g., a 15% difference at $\gamma = 0.1$). A small viscosity approximation of the threshold given by Müller *et al.* [8] also obtained the $\gamma^{3/2}$ correction for an infinite depth fluid. Finally, we note that a similar calculation for the damped Mathieu equation leads to a threshold $\gamma + 3\gamma^2/64 + O(\gamma^3)$, in which the first correction term is of a different order and has a different sign.

To derive the amplitude equation we use the multiple scale approach. The solvability condition in this case arises from the boundary conditions, not from the equation of motion as in most other cases. The velocity field is expanded as $\mathbf{u} = \epsilon^{1/2}\mathbf{u}_0 + \epsilon\mathbf{u}_1 + \epsilon^{3/2}\mathbf{u}_2 + \ldots$, with $\epsilon = (f - f_0)/f_0$, and similarly for p and ζ. Near threshold, i.e., for $\epsilon \ll 1$, we separate fast and slow time scales: $T = \epsilon t$; $\partial_t \to \partial_t + \epsilon\partial_T$. Spatial slow scales are not included because only regular patterns are considered here. At order $\epsilon^{1/2}$ we recover the linear solution discussed above. Because we are interested in standing wave patterns with different symmetries, the solution at this order is written as a linear combination of waves with wave vectors $\mathbf{k}_m$ of magnitude k_{onset} in different directions on

the x-y plane,

$$w_0 = \sum_m \cos(\mathbf{k}_m \cdot \mathbf{r}) B_m(T) \sum_{j=1,3,5,\ldots} e^{ji\omega t/2} w_0^j(z) e_j + \text{c.c.}$$

Here $B_m(T)$ are the *real* wave amplitudes, functions only of the slow time scale T, and e_j is denoted by A_j in Eq. (2).

At order ϵ the equation of motion and boundary conditions become

$$(\partial_t \nabla^2 - \nu \nabla^2 \nabla^2) w_1 = [\nabla \times \nabla \times (\mathbf{u}_0 \cdot \nabla)\mathbf{u}_0]_z ,$$

$$\partial_t \zeta_1 - w_1 = G_1(\mathbf{u}_0, \zeta_0) \quad \text{at } z = 0 ,$$

$$(\nabla_H^2 - \partial_z^2) w_1 = G_2(\mathbf{u}_0, \zeta_0) \quad \text{at } z = 0 ,$$

$$(3\nu \nabla_H^2 - \partial_t + \nu \partial_z^2)\partial_z w_0 + \left(g - \frac{\sigma}{\rho} \nabla_H^2 + f \cos \omega t \right) \nabla_H^2 \zeta_0 = G_3(\mathbf{u}_0, \zeta_0) \quad \text{at } z = 0 .$$

Here G_1, G_2, and G_3 are complicated functions of $\mathbf{u}_0$ and ζ_0. Note that the left-hand sides are identical to the equations at zeroth order with w_0 and ζ_0 replaced by w_1 and ζ_1. Since $[\nabla \times \nabla \times (\mathbf{u}_0 \cdot \nabla)\mathbf{u}_0]_z$ is of the form $\cos[(\mathbf{k}_m \pm \mathbf{k}_n) \cdot \mathbf{r}] e^{ji\omega t} Q(z)$, with $Q(z)$ consisting of various exponential functions, the particular solution w_{1p} can be obtained by integration. The homogeneous solution, $(\partial_t \nabla^2 - \nu \nabla^2 \nabla^2) w_{1h} = 0$, must be chosen to satisfy the boundary conditions. Because all these equations are very complicated, we have developed a symbolic manipulation program specific to this case, and found w_1 on a computer.

At order $\epsilon^{3/2}$ the equation of motion becomes

$$(\partial_t \nabla^2 - \nu \nabla^2 \nabla^2) w_2 = -\partial_T \nabla^2 w_0 + \{\nabla \times \nabla \times [(\mathbf{u}_0 \cdot \nabla)\mathbf{u}_1 + (\mathbf{u}_1 \cdot \nabla)\mathbf{u}_0]\}_z . \quad (3)$$

The boundary conditions are similar to those at first order with w_2 and ζ_2 on the left-hand sides and even more complicated functions of $(\mathbf{u}_0, \mathbf{u}_1, \zeta_0, \zeta_1)$ on the right-hand sides. Fortunately, only terms proportional to $\cos(\mathbf{k}_1 \cdot \mathbf{r})$ need to be considered in the solution for w_2 and ζ_2,

$$w_2 = \cos(\mathbf{k}_1 \cdot \mathbf{r}) \sum_{j=1,3,5,\ldots} \times e^{ji\omega t/2} [E_j + (a_j e^{kz} + b_j e^{q_j z}) C_j] ,$$

$$\zeta_2 = \cos(\mathbf{k}_1 \cdot \mathbf{r}) \sum_{j=1,3,5,\ldots} e^{ji\omega t/2} C_j .$$

Here $E_j(z)$ comes from the direct integration of Eq. (3), and $a_j e^{kz} + b_j e^{q_j z}$ is the homogeneous solution that has the same form as the linear solution, and C_j are constants to be determined later.

We first find (again with the symbolic manipulation program) a_j and b_j by using the kinematic and tangential stress boundary conditions at this order. The solution w_2 is finally inserted into the normal stress boundary condition at order $\epsilon^{3/2}$ to yield a system of equations for C_j which has the same left-hand side as Eq. (2) but with nonzero right-hand side. Solving for C_j just as in Eq. (2), we obtain $\bar{H}_1 C_1 - f_0 C_1^* = F$, with F a function of the amplitude B_m. Since $f_0 = |\bar{H}_1|$, by requiring a nontrivial solution for C_1 we obtain the solvability condition $F\bar{H}_1^* + F^* f_0 = 0$, which yields a standing wave amplitude equation,

$$\frac{dB_1}{dT} = \alpha B_1 - g_0 B_1^3 - \sum_{m \neg = 1} g(\theta_{m1}) B_m^2 B_1 , \quad (4)$$

with θ_{m1} the angle between $\mathbf{k}_m$ and $\mathbf{k}_1$, and explicit expressions for the coefficients. Equation (4) is of gradient form, and can be derived from a Lyapunov function,

$$\mathcal{F} = -\frac{1}{2} \alpha \sum_m B_m^2 + \frac{1}{4} \sum_m \sum_n g(\theta_{mn}) B_m^2 B_n^2 , \quad (5)$$

which may be used to find the preferred pattern near threshold [1]. For regular patterns of N standing waves, $\mathbf{k}_m$ form a regular polygon, and the B_m are constant.

We plot in Fig. 1 $g(\theta)/g_0$ for three different values of γ and $\Sigma = 1$ (capillary limit). For low γ, we observe that triad resonance leads to a peak at the resonant angle (see [10] for a more detailed discussion) that disappears as γ is increased. The figure shows that $g(\theta)/g_0$ at $\cos\theta = 0$ increases with increasing γ, so that the value at which the ratio crosses one delimits the region of stability of stripe patterns over square patterns.

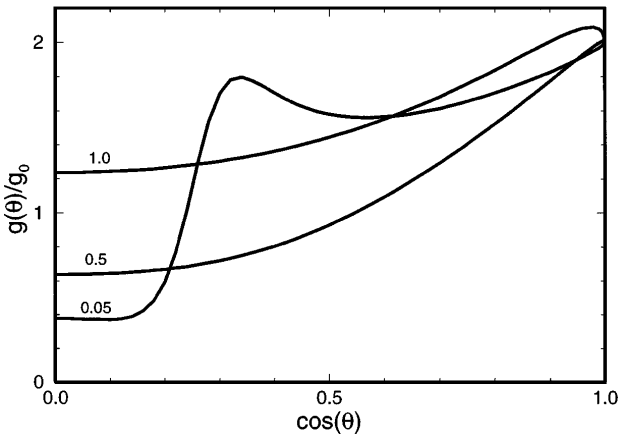

FIG. 1. Nonlinear coefficient of the standing wave amplitude equation $g(\theta)/g_0$ for $\gamma = 0.05$, 0.5, and 1.0, in the capillary limit $\Sigma = 1$.

We next turn to a comparison between the selected patterns predicted by Eq. (5) and two recent sets of systematic experimental surveys involving large aspect ratio systems, both of which aim at addressing the issue of pattern selection over a wide range of experimental parameters [4,5]. Binks and van de Water [5] have focused on a low viscosity fluid [13], a large aspect ratio cell, and a layer depth much larger than the wavelength. When the driving frequency is decreased from 45 Hz, a transition from a $N = 2$ square pattern to a $N = 3$ hexagonal pattern was observed at approximately 35 Hz, and to a quasiperiodic $N = 4$ eightfold pattern at approximately 29 Hz [14]. Our prediction for these transitions based on Eq. (5) are 35.4 and 28.7 Hz, respectively. These results are also in good agreement with the earlier weak damping calculation [10] that predicted the same transitions at frequencies of 32.8 and 27.9 Hz, respectively.

A large aspect ratio experiment involving fluids of various viscosities has been carried out by Kudrolli and Gollub [4]. Although the fluid depth (0.3 cm) is smaller than the wavelength in the experiment (1–3 cm), the comparison is still illuminating. Figure 2 shows the symmetry of the preferred patterns predicted by our calculations in the parameter space defined by the viscosity of the fluid and the driving frequency (with $\rho = 0.95$ g/cm^3 and $\sigma = 20.6$ dyne/cm), and the experimentally observed patterns. Stripe patterns are preferred at high viscosity, whereas at low viscosity, hexagons (at low frequency) and squares (at high frequency) are observed. We also show the small region in which a sequence of quasiperiodic patterns are expected to be selected. The experimental results by Kudrolli and Gollub are shown as the symbols in the figure. We note an excellent agreement in the regions in which stripes, squares, and hexagons are observed, specially in view of the shallow fluid depth involved in the experiment. The shallowness of the layer probably accounts for the observation of a hexagonal pattern at $\nu = 1$ cm^2/s and low frequency, and not observing a quasiperiodic pattern for $\nu = 0.04$ cm^2/s and $f = 27$ Hz. As noted above, the experiments by Binks and van de Water [5] did probe this latter region in a deep fluid layer, with their results agreeing with our predictions.

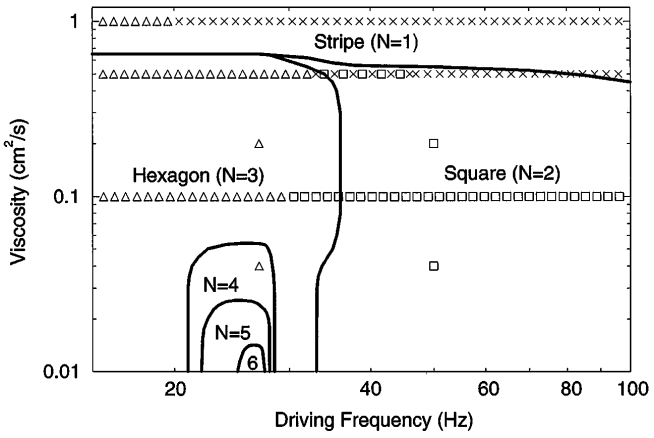

FIG. 2. Selected patterns as a function of the viscosity of the fluid and the angular frequency of the driving acceleration. The symbols represent experimental results: × = stripe pattern, □ = square pattern, and △ = hexagonal pattern. Alternating × and □ indicate mixed-stripe-square patterns.

Our calculations for parameter ranges outside those displayed in the figure indicate that the transition from square to stripe patterns upon increasing γ extends over the entire capillary wave range (high frequency limit in the experiment). However, stripe patterns are always preferred in the pure gravity wave limit (low frequency). We further point out that the logarithmic scale used in Fig. 2, as well as the small range of frequency probed account for the fact that stripe patterns seem to appear at roughly constant viscosity. The transition line separating square and hexagonal patterns is also close to a straight line because it is determined mainly by the value of G, which depends on the driving frequency but not on the viscosity.

This research has been supported by the U.S. Department of Energy, Contract No. DE-FG05-95ER14566, and also in part by the Supercomputer Computations Research Institute, which is partially funded by the U.S. Department of Energy, Contract No. DE-FC05-85ER25000.

[1] For a review, see M. C. Cross and P. C. Hohenberg, Rev. Mod. Phys. **65**, 851 (1993).
[2] See, e.g., N. B. Tufillaro, R. Ramshankar, and J. P. Gollub, Phys. Rev. Lett. **62**, 422 (1989); B. Christiansen, P. Alstrøm, and M. T. Levinsen, Phys. Rev. Lett. **68**, 2157 (1992); M. Torres, G. Pastor, I. Jiménez, and F. Montero de Espinosa, Chaos Solitons Fractals **5**, 2089 (1995); T. Besson and W. S. Edwards, Phys. Rev. E **54**, 507 (1996).
[3] W. S. Edwards and S. Fauve, Phys. Rev. E **47**, R788 (1993); J. Fluid Mech. **278**, 123 (1994).
[4] A. Kudrolli and J. P. Gollub, Physica (Amsterdam) **97D**, 133 (1996).
[5] D. Binks and W. van de Water, Phys. Rev. Lett. **78**, 4043 (1997).
[6] S. T. Milner, J. Fluid Mech. **225**, 81 (1991).
[7] J. W. Miles, J. Fluid Mech. **248**, 671 (1993); **269**, 353 (1994).
[8] H. W. Müller *et al.*, Phys. Rev. Lett. **78**, 2357 (1997).
[9] A. C. Newell and Y. Pomeau, J. Phys. A **26**, L429 (1993).
[10] W. Zhang and J. Viñals, Phys. Rev. E **53**, R4283 (1996); J. Fluid Mech. **336**, 301 (1997).
[11] H. Lamb, *Hydrodynamics* (Dover, New York, 1945), 6th ed.
[12] K. Kumar and L. S. Tuckerman, J. Fluid Mech. **279**, 49 (1994); K. Kumar, Proc. R. Soc. London A **452**, 1113 (1996).
[13] The fluid properties are $\nu = 0.03397$ cm^2/s ($\gamma \sim 0.01 - 0.03$), $\rho = 0.8924$ g/cm^3, and $\sigma = 18.3$ dyne/cm.
[14] In the experiment, patterns with $N = 5$ are observed at about 27 Hz. As it is also argued by the authors of the experiment, this could be attributed to finite size effects since $\mathcal{F}$ for $N = 5$ is larger but very close to $\mathcal{F}$ for $N = 4$. The difference at about 26 Hz is less than 0.2%.